Simulation of an avalanche in a fluid with a soft-sphere / immersed boundary method including a lubrication force.

Edouard Izard, Thomas Bonometti, Laurent Lacaze

Simulation of an Avalanche in a Fluid with a Soft-sphere/Immersed Boundary Method Including a Lubrication Force

Edouard Izard, Thomas Bonometti* and Laurent Lacaze
IMFT, Université de Toulouse, INPT, UPS, CNRS, Institut de Mécanique des Fluides de Toulouse, Allée Camille Soula, F-31400 Toulouse, France

Abstract

The present work aims at reproducing the local dynamics of a dense granular media evolving in a viscous fluid from the grain scale to that of thousands of grains, encountered in environmental multiphase flows. To this end a soft-sphere collision/immersed-boundary method is developed. The methods are validated alone through various standard configurations including static and dynamical situations. Then, simulations of binary wall-particle collisions in a fluid are performed for a wide range of Stokes number ranging in $[10^{-1}, 10^{4}]$. Good agreement with available experimental data is found provided that a local lubrication model is used. Finally, three- dimensional simulations of gravity/shear-driven dense granular flows in a viscous fluid are presented. The results open the way for a parametric study in the parameter space initial aspect ratio-initial packing.

1. INTRODUCTION

Particle-laden flows are encountered in a large number of industrial and natural applications, including chemical engineering, aeronautics, transportations, biomechanics, geophysics and oceanography. Modeling solid-fluid interaction is often difficult because of the complexity of the solid shape and motion in the fluid flow.

Methods for modeling solid-fluid interaction may be divided within two main groups, depending on the way the solid-fluid interfaces are described. One group, usually referred to as "body-fitted grid methods" makes use of a structured curvilinear or unstructured grid to conform the grid to the boundary of the fluid domain. In situations involving complex moving boundaries, one needs to establish a new body-conformal grid at each time-step leading to a substantial computational cost and subsequent slowdown of the solution procedure. In addition, issues associated with regridding arise such as grid-quality and grid-interpolation errors.

The second group of methods is referred to as "fixed-grid methods". These techniques make use of a fixed grid, which avoid any regridding procedure, while the presence of the solid objects is taken into account via adequately formulated source terms added to the fluid flow equations. Fixed-grid methods have emerged in recent years as a viable alternative to body-conformal grid methods. In this group, one can mention immersed-boundary method (IBM) [1-4], among others.

In the present work, we attempt to simulate the local dynamics of such systems from the grain scale to that of thousands of grains approximately. To this end a simple soft-sphere collision/immersed-boundary method is presented. The immersed-boundary method consists in a direct forcing method, using a continuous solid volume fraction to define the boundary. The granular media is modeled with a discrete element method (DEM) based on a multi-contact soft-sphere approach.

The paper is structured as follow. First we describe the numerical techniques used here, then preliminary test cases are presented to show the ability of both methods independently. In a third part, binary wall-particle collisions in a fluid are simulated for a wide range of Stokes number and a discussion about the use of a local lubrication model is done. Finally, three-dimensional simulations of dense granular flows in a viscous fluid are presented.

* Corresponding author: E-mail: thomas.bonometti@imft.fr

2. NUMERICAL APPROACHES

2.1 Immersed-boundary method (IBM)

Assuming a Newtonian fluid, the evolution of the flow is described using the Navier-Stokes equations, namely

$$\nabla \cdot \boldsymbol{V} = 0, \tag{1}$$

$$\rho \frac{\partial \boldsymbol{V}}{\partial t} + \rho \boldsymbol{V} \cdot \nabla \boldsymbol{V} = -\nabla p + \rho \boldsymbol{g} + \nabla \cdot \left[\mu \left(\nabla \boldsymbol{V} + {}^{t} \nabla \boldsymbol{V} \right) \right] + \rho f, \tag{2}$$

where $\boldsymbol{V}$, p, ρ and μ are the local velocity, pressure, density and dynamic viscosity in the flow, respectively, $\boldsymbol{g}$ denotes gravity and $\boldsymbol{f}$ is a volume force term used to take into account solid-fluid interaction. (1)-(2) are written in a Cartesian or polar system of coordinates. These equations are enforced throughout the entire domain, comprising the actual fluid domain and the space occupied by the particles. In the following, the term $\boldsymbol{f}$ will be formulated in such way as to represent the action of the immersed solid boundaries upon the fluid.

Let us consider a solid particle of density ρ_p, volume ϑ_p and mass m_p, the centroid of which being located at $\boldsymbol{x}_p$, moving at linear and angular velocity $\boldsymbol{u}_p$ and $\boldsymbol{\omega}_p$, respectively. The local velocity $\boldsymbol{U}$ in the object is then defined by $\boldsymbol{U} = \boldsymbol{u}_p + \mathbf{r} \times \boldsymbol{\omega}_p$, $\mathbf{r}$ being the local position relative the solid centroid. The motion of the particle is described by the Newton's equations for linear and angular momentum of a rigid body, *viz* [4]

$$m_p \frac{d\boldsymbol{u}_p}{dt} = m_p \boldsymbol{g} + \boldsymbol{F}_h, \tag{3}$$

$$\boldsymbol{I}_p \frac{d\omega_p}{dt} = \boldsymbol{\Gamma}_h, \tag{4}$$

$$\boldsymbol{F}_h = -\frac{\rho \rho_p}{\left(\rho_p - \rho \right)} \int_{\vartheta_p} \boldsymbol{f} d\vartheta, \tag{5}$$

$$\boldsymbol{\Gamma}_h = -\frac{\rho \rho_p}{\left(\rho_p - \rho \right)} \int_{\vartheta_p} \boldsymbol{r} \times \boldsymbol{f} d\vartheta, \tag{6}$$

where $\boldsymbol{F}_h$ (resp. $\boldsymbol{\Gamma}_h$) is the acceleration (resp. torque) due to hydrodynamic forces.

The time integration of the momentum equations for the fluid (2) and the solid (3-4) is performed via a third-order Runge-Kutta method for all terms except the viscous term for which a second-order semi-implicit Crank-Nicolson scheme is used. The incompressibility condition (1) is satisfied at the end of each time step through a projection method. Domain decomposition and Message Passing Interface (MPI) parallelization is performed to facilitate simulation of large number of computational cells. The detailed description of the resolution of (1)-(2) is given in [5] and will not be repeated here.

In general, the location of the particle surface is unlikely to coincide with the grid nodes, so that interpolation techniques are usually employed to enforce the boundary condition by imposing constraints on the neighboring grid nodes (see [4] for instance). Here we adopt another strategy, by introducing a function α denoted as "solid volume fraction", which is equal to one in cells filled with the solid phase, zero in cells filled with the fluid phase, and $0 < \alpha < 1$ in the region of the boundary. In practice, the transition region is set-up to be of one-to-three grid cells approximately [6]. The forcing term then reads

$$\boldsymbol{f} = \alpha \frac{\boldsymbol{U} - \boldsymbol{V}}{\Delta t}. \tag{7}$$

Recall that $\boldsymbol{U}$ is the local velocity obtained from (3)-(4) and imposed to the immersed solid object while $\boldsymbol{V}$ is the predictive local velocity found for the fluid without considering the solid object; Δt is the time step used for the time-advancement. The present choice, which may be viewed as a smoothing of the immersed boundary, is an alternative way to using a regularized delta function in conjunction with a Lagrangian marking of the boundary. The latter technique is largely used in immersed-boundary methods in order to allow for a smooth transfer of momentum from the boundary to the fluid (see e.g. [2, 4]). The advantage of the present choice is that it is simple to implement and no interpolation is performed so that the computational cost is reduced.

In the following, spherical particles will be considered. The corresponding solid volume fraction α is defined by [6],

$$\alpha(x) = \frac{1}{2} - \frac{1}{2}\tanh\left(\frac{\left|\boldsymbol{x} - \boldsymbol{x}_p\right| - R}{\lambda\sigma\Delta}\right), \tag{8}$$

$$\lambda = \left|n_x\right| + \left|n_y\right| + \left|n_z\right|, \tag{9}$$

$$\sigma = 0.065\left(1 - \lambda^2\right) + 0.39, \tag{10}$$

where $\boldsymbol{n} = (n_x, n_y, n_z)$ is a normal outward unit vector at a surface element, σ is a parameter controlling the thickness of the transition region and Δ is a characteristic grid size ($\Delta = 2^{1/2}\,\Delta x$ when the grid is uniform). More explicitly, in a grid cell, the unit vector $\boldsymbol{n}$ is simply computed using the location of the sphere center and that of the local grid cell, since here we only consider spheres. Iso-contours of α as defined in (8) are shown in the inset of figure 2. With the present choices, the transition region is of three grid cells approximately.

2.2 Soft-sphere approach (DEM)

As shown later, the coupled IBM-DEM method may not be accurate in capturing the detailed flow structure in the liquid film that is drained when the particles approach each other because of the somewhat limited spatial resolution of the flow in the narrow gap. Moreover, solid particles may collide through solid-solid interaction if their inertia overcome dissipative effects induced by the above mentioned drainage flow. In these specific cases, equations (3)-(4) have to be modified to incorporate the resulting interaction forces. In this section, we describe the discrete element method (DEM) developed here to deal with these local forces in the case of multi-grain interactions.

2.2.1 Solid-solid interaction

We first describe the method used for dealing with solid contacts in a system of n_p particles which is based on a standard DEM approach described in [7]. Here, the modeling of the solid-solid interaction is done via a soft-sphere approach. Briefly, we assume the particles to be non-deformable but being able to overlap each other. This overlap is then used to compute the normal and tangential contact forces, using a local linear mass-spring system and a Coulomb type model, respectively. When coupling is performed, an extra force $\boldsymbol{F}_c$ and torque $\boldsymbol{\Gamma}_c$ is added in (3) and (4) for each particle labeled i, namely

$$\boldsymbol{F}_c = \sum_{j \neq i} \boldsymbol{F}_{i-j} + \boldsymbol{F}_{wall}, \tag{11}$$

$$\boldsymbol{\Gamma}_c = \sum_{j \neq i} \boldsymbol{\Gamma}_{i-j} + \boldsymbol{\Gamma}_{wall}, \tag{12}$$

where $\boldsymbol{F}_{i\text{-}j}$ is the contact force between particles i and j, $\boldsymbol{F}_{wall}$ the wall-particle interaction force, $\boldsymbol{\Gamma}_{i\text{-}j}$ and $\boldsymbol{\Gamma}_{wall}$ are the corresponding torques. $\boldsymbol{F}_{i\text{-}j}$ and $\boldsymbol{\Gamma}_{i\text{-}j}$ are computed using a local system of coordinates $(\boldsymbol{n}, \boldsymbol{t})$ depicted in figure 1 as follows

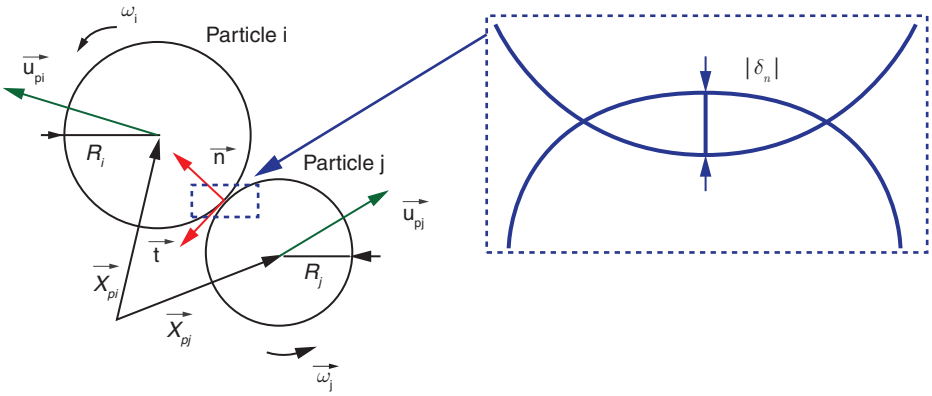

Figure 1: Sketch of a typical particle-particle collision and notations used in the soft-sphere approach.

$$\boldsymbol{F}_{i-j} = F_n \boldsymbol{n} + F_t \boldsymbol{t} \tag{13}$$

$$\omega_{i-j} = R_i \boldsymbol{n} \times F_t \boldsymbol{t} \tag{14}$$

$$F_n = \begin{cases} 0 \quad \text{if} \quad \delta_n > 0 \\ \max\left(0, -k_n \delta_n - \gamma_n \dfrac{d\delta_n}{dt}\right) \quad \text{otherwise}, \end{cases} \tag{15}$$

$$F_t = -\min\left(\left|k_t \delta_t\right|, \left|\mu_c F_n\right|\right) sign\left(\delta_t\right), \tag{16}$$

where R_i is the i-th particle radius, δ_n (δ_t) is the normal (tangential) distance of overlap, μ_c is the friction coefficient, k_n (resp. k_t) is the normal (resp. tangential) stiffness and γ_n is the damping coefficient of the mass-spring model. Note that $\boldsymbol{F}_{wall}$ and $\boldsymbol{\Gamma}_{wall}$ are treated in a similar manner by taking an infinite radius and mass for the wall. The constants of the mass-spring model γ_n, k_n and k_t are calculated thanks to two additional parameters, namely the coefficient of normal restitution e_n and the contact time t_c. These quantities are characteristic of the elastic properties of the particles.

$$\gamma_n = -\frac{2m_*}{t_c} \ln\left(e_n\right), \tag{17}$$

$$k_n = \frac{m_* \pi^2}{t_c^2} + \frac{\gamma_n^2}{4m_*}, \tag{18}$$

where $m_* = m_i m_j / (m_i + m_j)$ is the effective mass involved in the contact. Finally, the tangential stiffness coefficient k_t is assumed to be proportional to the normal stiffness coefficient k_n [8]. In the present work, we set $k_t = 0.2 k_n$. To summarize, in the present soft-sphere approach, one needs to specify e_n, t_c and μ_c in addition to the size and density of the particles for the model to be closed.

2.2.2 Lubrication force

As mentioned above, the lubrication force induced by approaching spheres can become dominant prior solid contact, while the IBM method is not able to accurately describe the flow on such short distance of interactions (generally smaller than the grid size). An extra lubrication force may therefore be added in (3) to compensate for this [9]. Here we use the following model of lubrication force [10] between two approaching particles i and j of velocity $\boldsymbol{u}_{p,i}$ and $\boldsymbol{u}_{p,j}$ and radius R_i and R_j,

$$\boldsymbol{F}_{lub} = -\frac{6\pi\mu\left(\boldsymbol{u}_{pi}.\boldsymbol{n} - \boldsymbol{u}_{pj}.\boldsymbol{n}\right)}{\delta_n + \eta}\left(\frac{R_i R_j}{R_i + R_j}\right)^2 \boldsymbol{n}, \tag{19}$$

where η is an effective roughness length accounting for the roughness height of real grains. This parameter is added in the model in order to mimic real particles roughness and avoid the divergence of the force when contact occurs ($\delta_n = 0$). Depending on the type of material used for the particles, the relative roughness height η/R is roughly in the range $[10^{-6}; 10^{-3}]$ (see e.g. Ref [11]). The present lubrication force is used when the distance between particles is in the range $0 \le \delta_n \le R/2$. We checked that the specific value of the upper bound of the force application (within the range $[\Delta x; R]$) does not affect the results significantly. Results with the lubrication force (19) are presented in figures 6-7 and 8-9, which will be detailed in section 4.

3. PRELIMINARY TESTS WITHOUT COUPLING

3.1 Falling sphere in a viscous liquid initially at rest

We set the physical properties of the particle and the fluid so the density ratio is $\rho_p/\rho = 4$ and the Archimedes number $Ar = \rho(\rho_p - \rho)gD^3/\mu^2 = 800$. As shown later, this corresponds to a Reynolds number, based on the terminal velocity of the sphere, of $Re = \rho u_p D/\mu = 20$ approximately, for which the wake flow is axisymmetric leading to a rectilinear trajectory of the falling particle. Here, we compare our results with those of a boundary-fitted approach which has been validated in previous papers [12]. This method fully resolves the flow around the falling sphere in the reference frame of the moving object, thanks to a spherical curvilinear grid which is refined in the vicinity of the rigid boundary. The particle motion is solved via the Kirchhoff equations of motion. In this method a $88 \times 34 \times 66$ spherical grid was used and the outer boundary was located at a distance of $20D$ from the sphere center.

In the present case, the simulation is performed in a cylindrical computational (r, z)-domain of $20D \times 40D$ size with a 128×800 grid points. The spatial resolution is constant along the z-direction parallel to gravity as well as in the region $0 \le r/D \le 1.5$ ($D/\Delta x = 20$). For $1.5 \le r/D \le 20$, the grid size is varied following an arithmetic progression up to the outer wall. Free-slip boundary conditions are imposed at all boundaries. The time-step used for the simulation is $\Delta t(g/D)^{1/2} = 0.04$. Inset of figure 2 shows the grid used and iso-contours of the solid volume fraction α defined in (8). Initially, the sphere is located at a distance $5R$ from the upper wall and the fluid is at rest.

One can estimate the initial acceleration of the sphere at early times, assuming that only the buoyancy force and the added-mass force are at play. The initial vertical acceleration reads

$$\frac{du_p}{dt} = \frac{\left(\rho_p - \rho\right)g}{\rho_p + C_M \rho}, \tag{20}$$

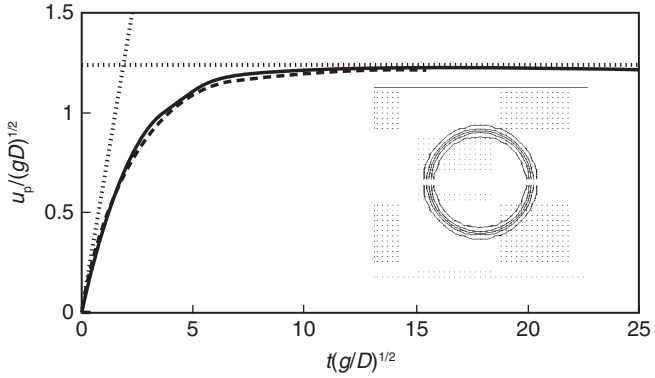

Figure 2: Time evolution of the particle velocity: —, present IBM method, - - -, boundary-fitted approach [12], ·····, analytical solutions (20)-(21). Inset: close-up view of the grid used for the IBM simulation, with iso-contours of α = 0.01, 0.25, 0.5, 0.75 and 0.99.

where C_M is the added-mass coefficient equal to 1/2 for a sphere. When the sphere has reached a terminal velocity, the drag force is balanced by the buoyancy force so the terminal velocity can be computed as follows

$$u_p = \sqrt{\frac{|m_p - m|g}{\frac{1}{2}C_D \rho \pi R^2}}, \tag{21}$$

where m_p and m are the mass of the spherical particle and the mass of the fluid contained in the same volume, respectively. C_D is the drag coefficient which can be classically estimated using Schiller and Naumann's correlation [13]. Using this correlation together with the definition of the Reynolds number $Re = \rho \mu_p D/\mu$ and (21), one can determine the theoretical terminal velocity of the sphere. Figure 2 shows the temporal evolution of the sphere velocity with the boundary-fitted approach and the present immersed boundary method. For comparison, analytical solutions (20) and (21) are also plotted. Excellent agreement is observed with respect to both the numerical and analytical solutions. The present method is shown to satisfactorily reproduce the dynamics of a free-moving object in a viscous fluid, from the acceleration phase up to the steady-state regime.

3.2 Binary collision between two spheres

Binary collisions between two spheres have been investigated through experiments [8] and DEM simulations [14], in the limit of no-effect of the surrounding fluid. In Ref [8], Foester et al. measured, for different materials, the tangential component of the relative velocity before (Ψ_1) and after (Ψ_2) impact, normalized by the normal component of the relative velocity before impact.

The soft-sphere approach presented in section 2 is used, considering only "dry collisions", that is we solve (3) after having removed $\boldsymbol{F_h}$ and $\boldsymbol{\Gamma_h}$ and introduced solid-solid contacts $\boldsymbol{F_c}$ and $\boldsymbol{\Gamma_c}$, respectively. In the present case, we compute the collision between two acetate spheres of radius $R = 1.5 \times 10^{-3}$m. Material properties are $\rho_p = 1319$ kg.m^{-3}, $\mu_c = 0.25$, $e_n = 0.87$ as in the experiments of [8]. Moreover, t_c is set to 10^{-5}s.

The evolution of Ψ_2 as a function of Ψ_1 obtained from the present soft sphere method is shown in figure 3 together with experiments of [7]. Good agreement is observed. The first part of the curve ($\Psi_1 < 1.5$) corresponds to a change of sign of the tangential velocity during contact due to the elasticity of the material. During the collision, the spheres partially slip on each other. For $\Psi_2 = 0$, slip-free rolling exists. The positive linear part ($\Psi_1 > 1.5$) corresponds to slip. In that case, the Coulomb criterion is verified during all the contact duration. Overall, the present soft-sphere method is able to quantitatively reproduce experimental observations of binary collisions in the dry case.

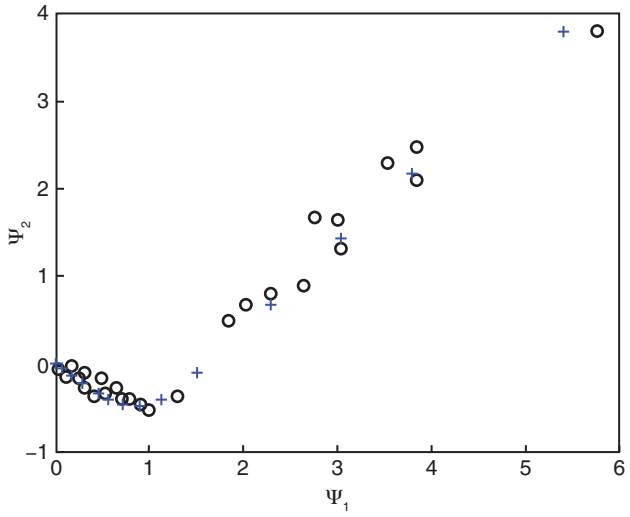

Figure 3: $_2$ as a function of $_1$ in the case of dry binary collisions. O: experiments of [8]; + present soft sphere method.

3.3 Granular pressure in a silo

Again, only solid-solid interactions are considered here, using the soft sphere approach. This test case correspond to the filling of a silo of dimension 0.1 × 0.1 × 5m (figure 4) by 56000 particles of density $\rho_p = 1317$ kg.m^{-3} and mean radius $R = 5$ mm under gravity g = 9.81 m/s^2. The radius is varied from one particle to another in a range of ±10% to avoid crystallization phenomena. Here we set the collision parameters to $\mu_c = 0.25$, $e_n = 0.3$ and $t_c = 10^{-4}$s. The walls were covered by fixed particles of equivalent size as those injected in the silo.

When the granular column is at rest, a coarse-graining technique is applied (see e.g. [15]) to measure the local granular stress tensor and the subsequent granular pressure (spherical part of the tensor). We plot in figure 4 the horizontally-averaged granular pressure in the silo. Going from the top of the column ($z \approx 5$m) down to the bottom ($z = 0$m), the granular pressure first follows a "hydrostatic" linear distribution on a depth corresponding to one silo diameter (4.9m $\leq z \leq$ 5m), then the pressure quickly reaches a plateau and remains roughly constant on a distance of 4m down to $z \approx 0.7$m. Below this height, the pressure monotonously increases as one gets to the bottom boundary. This behavior is attributed to the fact that in this region, particles have interacted with the bottom wall so the friction with the vertical wall was reduced and the pressure increased accordingly.

The prediction of the granular pressure in the silo has been the subject of considerable work because of its obvious practical interest. One conventional model, namely the Janssen model, has proved to reproduce reasonably well the pressure distribution in a silo. In this model one assumes that (i) the grain assembly is a continuous medium of equivalent density $\rho_{gm} = C\rho_p$, C being the global compactness in the granular column, (ii) the vertical stresses are redistributed toward the horizontal directions by a factor K and (iii) the wall friction is at the threshold of motion. Under these assumption, the vertical distribution of the granular pressure reads,

$$p(z) = \frac{\rho_{gm} g S}{f_w K P}\left(1 - e^{\frac{f_w K P}{S}(h-z)}\right), \tag{22}$$

where S (P) is the horizontal cross-section (perimeter) of the silo, fw is the wall friction coefficient, K is the coefficient of stress redirection and h is the height of the granular column. Note that the coarse-graining technique allows us to directly measure f_w and K while these quantities are difficult

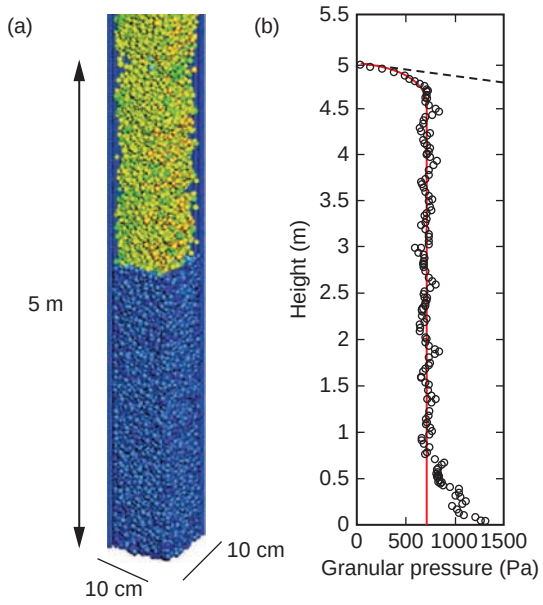

Figure 4: Soft-sphere simulation. (a) Silo filling with 56000 particles colorized by their velocity (blue: low velocity, red: high velocity). (b) Horizontally-averaged granular pressure distribution in the silo (when the granular medium is at rest): O, present DEM method, —, analytical solution (22), - - -, equivalent hydrostatic distribution.

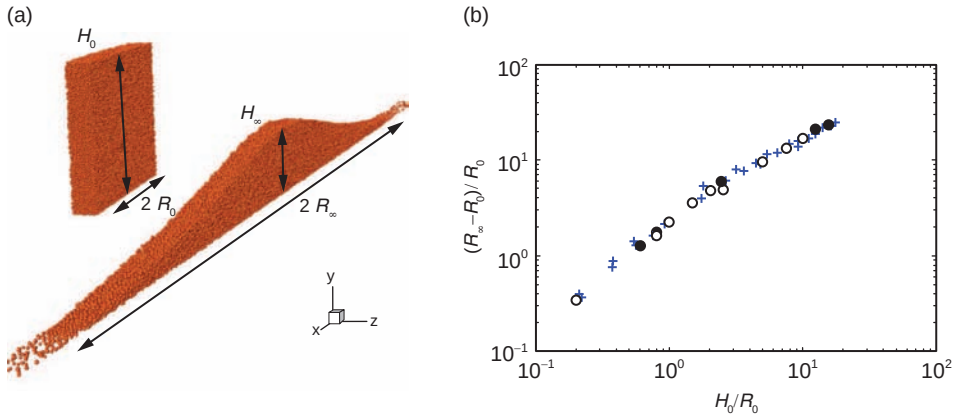

Figure 5: Collapse of a granular column. (a) Initial and final configurations. (b) Dimensionless distance of run-out as a function of initial aspect ratio: ●, present DEM method (2D); O, present DEM method (3D); +, two-dimensional DEM simulations of [16].

to determine a priori or in a real experiment. Therefore, we plotted in figure 4 the analytical solution (22) by estimating the parameter $f_w K$ using a best fit of the numerical results. This gives a value of $f_w K \approx 0.30 \pm 0.06$. The direct calculation of $f_w K$ from the numerical data gives, including the dispersion error, $f_w K \approx 0.38 \pm 0.11$, a value which is in reasonable agreement with the best-fit estimate. This shows the capability of the present soft-sphere method to accurately reproduce the behavior of a dense granular media at rest.

3.4 Collapse of a granular column

The collapse of a granular column of height H_0 and half-length R_0 is a common academic configuration used to provide empirical laws of the final deposit of geophysical granular systems (figure 5). Assuming the ambient fluid plays no role in the dynamics, DEM methods have been shown to be an efficient tool to simulate this configuration [16-18].

Here, the soft-sphere method is used for simulating two- and three-dimensional dry granular collapses under gravity g = 9.81 m/s^2 in planar configurations. We use 7×10^3 to 120×10^3 (resp. 10^3 to 8×10^3) spheres in our 3D (resp. 2D) columns (figure 5a). Material properties are $\rho_p = 2500$ kg.m^{-3}, $e_n = 0.5$, $t_c = 10^{-4}$s and $R = 5$ mm. Again, the radius is varied from one particle to another in a range of 10% to avoid crystallization phenomena. The friction coefficients between spheres and between a sphere and the wall were set to $\mu_c = 1$. Columns were always filled following the same protocol consisting of the sedimentation of particles, initially at rest, randomly placed in the computational domain bounded by walls. In the 2D case all frontiers are walls, while in the 3D cases, periodic conditions are imposed in the spanwise direction z. The initial column is filled up to a height H_0 in a box of horizontal length $2R_0$. In the 3D case, the domain has a spanwise length of 12D. At time $t = 0$, the two vertical walls are removed and the granular column symmetrically collapses on the horizontal plane. Snapshots of the granular media in the initial and final state are shown in figure 5a. When the particles are at rest, we measure the final height H_∞ and length R_∞.

The normalized final deposit, referred to as the run-out distance defined as $(R_\infty - R_0)/R_0$, is plotted in figure 5b as a function of the initial aspect ratio $a = H_0/R_0$. Comparisons are made with two-dimensional simulations of [16] who used a contact-dynamic method and found good agreement with experiments. Both models give the same final deposit and corresponding scaling laws. Interestingly, three-dimensional effects do not seem to influence the run-out distance. We conclude that the dynamics of the granular flow is well capture by the present method.

4. RESULTS

In the following, the immersed boundary method (IBM) is coupled with the soft-sphere approach (DEM). Assuming the characteristic contact time step t_c to be much smaller than the characteristic fluid time scale t_f, we separately solve equations (1)-(2) and (3)-(4), adding (11) and (19) in (3) as

source terms (and the corresponding torques accordingly). The fluid velocity and pressure are computed with the IBM approach, and then hydrodynamic forces and torques on each particle are computed and sent to the DEM code, which computes the new position and velocity of the particles on several solid time steps up to the fluid time step which can be chosen here larger that the solid time step since one assumes $t_f >> t_c$, and taking into account possible contacts and lubrication force. The position and velocity of the particles is then sent back to the IBM solver.

4.1 Bouncing of a solid sphere on a wall in a viscous fluid

In this section, we present results of the simulation of one spherical particle bouncing on a wall in a viscous liquid initially at rest. The simulation is performed with the same grid as that shown in figure 2. Here the resolution is $D/\Delta x = 20$. Note that tests with $D/\Delta x = 10$ and 40 have been done and showed that the results were not affected by spatial resolution in the range considered here. Free-slip boundary conditions are imposed at all boundaries except at the bottom wall where bouncing occurs, for which a no-slip condition is applied. We set the physical properties of the particle and the fluid so that we cover a range of density ratios $2 \le \rho_p/\rho \le 10^2$, Reynolds numbers $0.1 \le Re = \rho u_p D/\mu \le O(10^2)$ and Stokes numbers $1 \le St \le 10^4$. Here Stokes number is defined as,

$$St = \frac{\left(\rho_p + C_M \rho\right) V_T \, D}{9\mu}, \tag{23}$$

where $C_M = 1/2$ is the added-mass coefficient of a spherical particle.

The evolution of the vorticity field around the particle during impact is presented in figure 6, for the case $\rho_p/\rho = 8$, $St = 53$ and $Re \approx 60$. Here the collision parameters were set to $e_n = 0.97$, $t_c = 10^{-4}$s, $\mu_c = 0.25$, and the relative roughness height used in the lubrication model (19) was set to

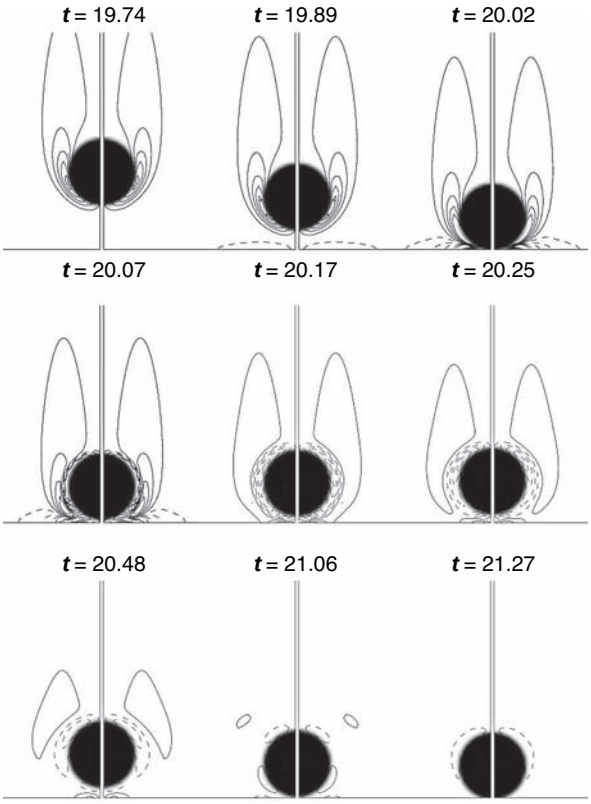

Figure 6: Vorticity field around a sphere impacting a wall ($\rho_p/\rho = 8$, $St = 53$, $Re \approx 60$, $D/\Delta z = 20$.). Contour levels are set from –17.8 to 17.8 in increments of 3.9. Here, time and vorticity are scaled by $(D/g)^{1/2}$ and $(g/D)^{1/2}$, respectively.

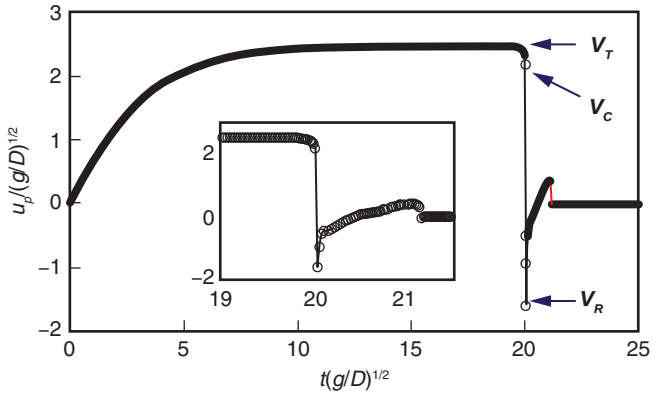

Figure 7: Temporal evolution of the particle vertical velocity (same case as figure 6). Inset: close-up view of the velocity during bouncing. Also defined are the particle terminal velocity V_T, the velocity at contact V_C and the rebound velocity V_R.

$\eta/R = 4 \times 10^{-4}$. In the following, time is scaled by $(D/g)^{1/2}$. At $t = 19.74$, the flow field around the particle is not influenced by the wall and vice versa. However, when the sphere gets closer to the wall, the fluid is pushed away from the centerline and vorticity is created at the wall. This is visible in figure 6 at time $t = 19.89$ as the particle is at a distance from the wall of R approximately. Note that at this time instance, the grid resolution is of 4-5 grid cells in the liquid film. When collision occurs at $t = 20.02$ ($\delta_n \leq 0$), vorticity is maximum in the region close to the impact zone, indicating strong shear stress as fluid is pushed away parallel to the wall. Right after impact ($20.07 \leq t \leq 20.25$) a thin layer of vorticity of opposite sign develops at the particle surface and at the wall, while vorticity in the wake of the particle decreases, though still present. At $t = 20.48$, the particle has reached its maximum height after the first bouncing and falls back again toward the wall. Afterwards ($t \geq 21.06$), the vorticity around the particle quickly disappear because of significant viscous dissipation.

The corresponding time evolution of the particle velocity is displayed in figure 7. Clearly, the particle reaches a steady-state velocity, denoted V_T, before bouncing on the wall. It can be noticed that before the collision effectively occurs the particle velocity decreases from V_T to an impact velocity, denoted V_C, which is about 12% less than V_T in the present case. During the bouncing, the particle velocity changes sign but does not recover its initial velocity. This rebound velocity is denoted V_R. Right after the impact, there is a strong decrease of the particle velocity followed by a milder trend. Finally, one can see on figure 7 a second rebound ($t \approx 21$), which is hardly detectable from the flow visualization.

The simulation presented in figures 6 and 7 were first repeated for two specific density ratios $\rho_p/\rho = 8$ and 16 (St and Re varying in the abovementioned range) and one specific Reynolds number $Re = 1$, without any lubrication model (19). We plot in figure 8 the restitution coefficient $e/e_n = -V_R/V_T$ (see figure 7 for definitions) as a function of Stokes number (23). For comparison, we included available experiment data of the rebound of a spherical inclusion with a wall or another particle. While the numerical results are in good agreement with experimental data for $St \geq 200$, the restitution coefficient is clearly overestimated at lower St. This can be attributed to the low resolution of the flow field when the gap between the particle and the wall is of the order of the grid size. As a consequence, the film pressure stemming from the drainage of the liquid in the gap is underestimated so the particle rebound is artificially enhanced. This issue is overcome when one adds a lubrication force (19) in (3). Figure 9 shows the results obtained with the coupled IBM- DEM method with the lubrication model (19) for the case $\rho_p/\rho = 8$. The numerical results fall in the range of the experimental data.

Overall, one may conclude from figure 9 that the present IBM-DEM method is able to reproduce the rebound of a particle in a viscous fluid provided a suitable lubrication model is added to compensate the inability of the flow solver to capture the small scale flow field in the gap during the film drainage.

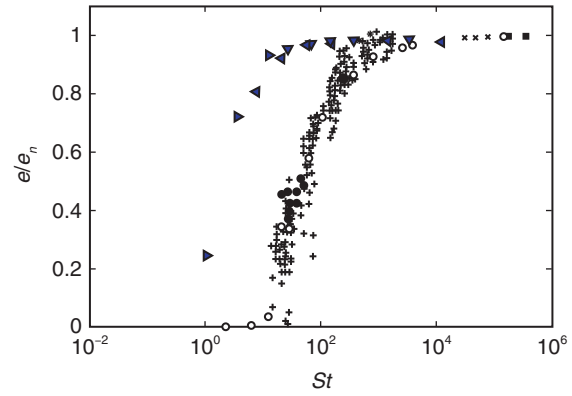

Figure 8: Restitution coefficient *e/en* for spherical inclusions versus the Stokes number St. Present IBM-DEM simulations without lubrication force: T, $\rho_p/\rho = 16$; ◀, $\rho_p/\rho = 8$; ▶ $Re_p \approx 1$. Experiments with solid spheres: +, Joseph et al. [11]; O, Gondret et al. [19]; ×, Foerster et al. [8]. Experiments with drops: •, toluene drops in water (Legendre et al. [20]); ♦, liquid drop in air (Richard & Quéré [21]). Other experiments: ■, spherical balloon filled with a mixture of water and glycerol (Richard & Quéré [21]).

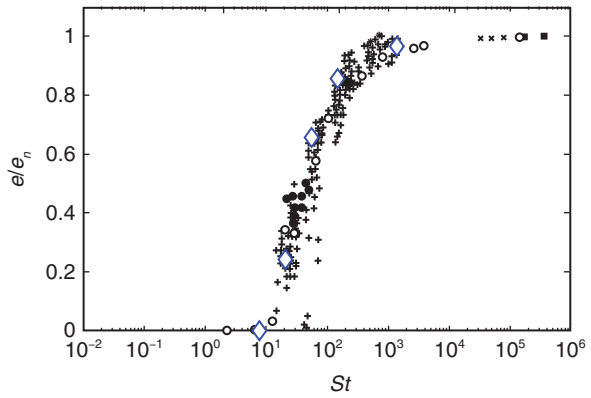

Figure 9: Same as figure 8: ♦, present IBM-DEM simulations with lubrication force (19) for $_p/$ = 8 and a various relative roughness height /$R = 2 \times 10^{-4}$.

4.2 Immersed granular flow on an inclined plane

The final case corresponds to the simulation of an immersed granular flow on an inclined plane. The simulation is performed in a three-dimensional (x,y,z)-computational domain of size 10D × 3D × 10D in the streamwise, spanwise and vertical directions, respectively, discretized with 100 × 30 × 100 grid points (figure 10a). We set the physical properties of the particle and the fluid so the density ratio is $\rho_p/\rho = 8$ and the Archimedes number $Ar = \rho(\rho_p-\rho)gD^3/\mu^2 \approx 9$. This choice leads to an a posteriori value of Stokes number of 0.5 and Reynolds number $\mathrm{Re} = \rho u_p D/\mu \approx 10$, approximately. Hence, one expects the present granular flow to be in the viscous limit regime according to Courrech Du Pont et al.'s classification [22] (as shown in figure 10b). The collision parameters are $e_n = 0.87$, $t_c(g/D)^{1/2} = 4.5 \times 10^{-3}$, $\mu_c = 0.25$, and the relative roughness height used in the lubrication model (19) is set to $\eta/R = 4 \times 10^{-4}$. Periodic boundary conditions are imposed in the streamwise x- and spanwise y-direction, while a no-slip (resp. free-slip) boundary condition is imposed at the bottom wall (resp. top wall). The gravity vector makes an angle β of 22° with the z-direction in the (x, z)-plane. Thirty half-spheres are fixed at the bottom wall in order to resemble natural rough bottoms, while 200 quasi-monodispersed moving particles are initially positioned as in a settling bed of grains, the fluid being initially at rest. Note that with the present angle of inclination, the bed of grain would have been motionless if there were no fluid flowing down.

Depending on the angle of inclination and the properties of both the solid phase and the fluid phase, the granular flow can be either driven by gravitational forces (avalanche) or shear induced

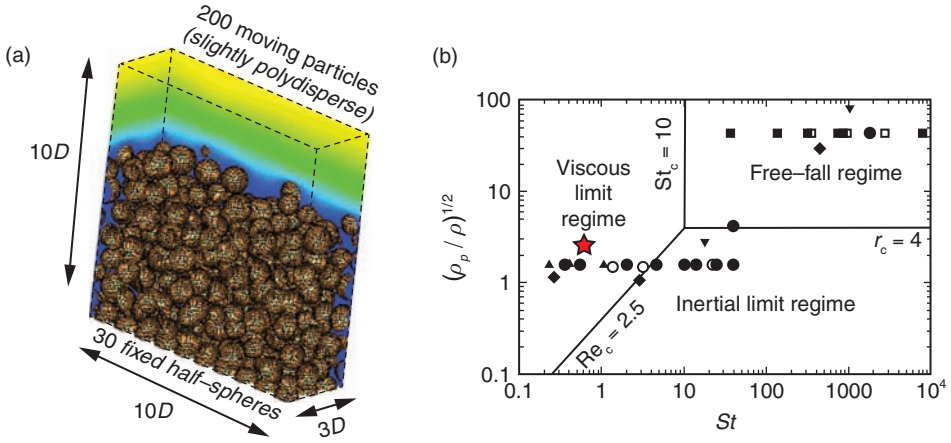

Figure 10: (a) Numerical setup of the simulation of the gravity/shear-driven granular flow. (b) Regime of the granular flow according to Courrech Du Pont et al.'s classification [22]: ☆, present simulation; other symbols, experiments of [22].

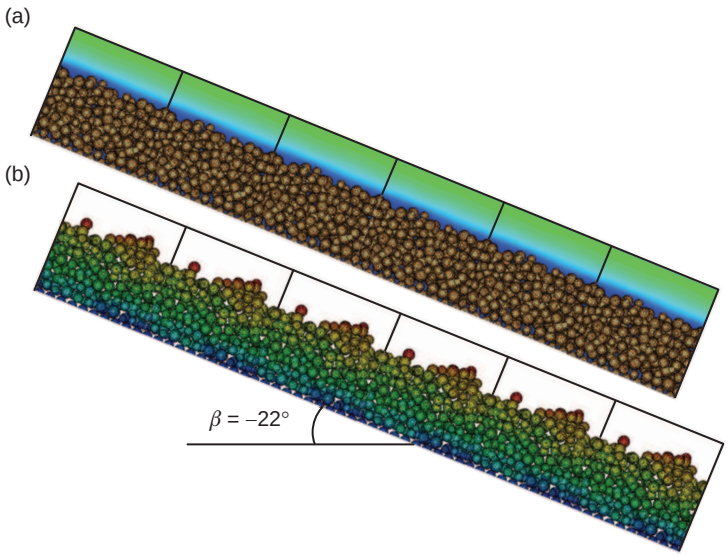

Figure 11: Topology of the bed of grains at (a) $t(g/D)^{1/2} \approx 10$, and (b) $t(g/D)^{1/2} \approx 256$.The computational domain is represented by the gray lines. In (a) (resp. (b)), the background (resp. bed of grains) is colored by the local streamwise velocity of the fluid (blue: low values; red: large values).

by the fluid at the surface of the bed of grains (erosion). In the present configuration, the temporal evolution of the granular flow is as follow: the fluid is first put into motion due to gravity and the presence of periodic boundary conditions, creating a boundary layer at the surface of the static granular bed (figure 11a). When shear is large enough, the upper layer of particles starts to move, entraining the lower layers of grains step by step. At some point, the whole bed of grains is abruptly put in motion (at $t(g/D)^{1/2} \approx 50$), indicating the triggering of an avalanche (not shown). At later times, $t(g/D)^{1/2} \geq 100$, the height of the bed becomes inhomogeneous and exhibits patterns looking like ripples, the amplitude of which being of 2-3 particle diameters and the wavelength being of the size of the computational box (figure 11b). Obviously, simulations in a larger domain are needed to obtain quantitative prediction of the growth-rate and most unstable wavelength of the instability of the bed surface.

In figure 12, we plot the particles and fluid mean streamwise velocity as a function of height for three spatial resolutions, namely $D/\Delta x = 5$, 10 and 15. Here, a spatial averaging is made in

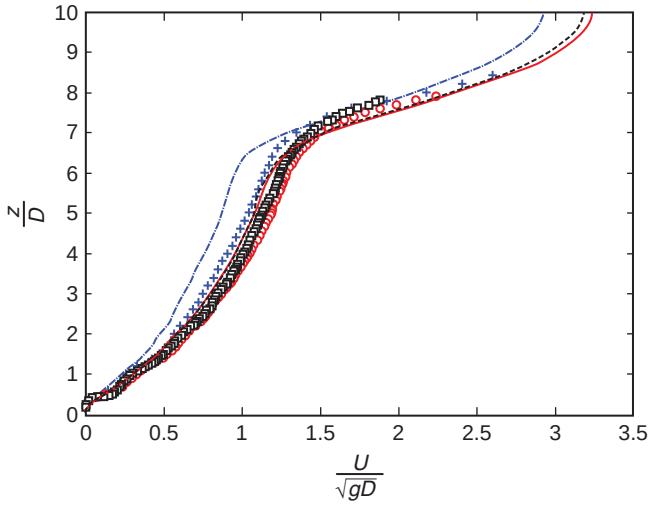

Figure 12: Particles (symbols) and fluid (lines) mean streamwise velocity as a function of height for three spatial resolutions: - - - (blue), grid 50 × 15 × 50 ($D/\Delta x$ = 5); —(red), grid 100 × 30 × 100 ($D/\Delta x$ = 10); - - - (black), grid 150 × 45 × 150 ($D/\Delta x$ = 15). Spatial averaging is made in horizontal planes and time averaging is done from $t(g/D)^{1/2} \approx 200$ to $t(g/D)^{1/2} \approx 350$. For the highest resolutions, the maximum difference in velocity is of 1.6% (resp. 11.5%) for the fluid (resp. granular) phase.

horizontal planes and a time averaging is done from $t(g/D)^{1/2} \approx 200$ to$t(g/D)^{1/2} \approx 350$. The velocity profiles for the two highest resolutions are close to one another, the maximum difference in velocity being of 1.6% for the fluid phase. This indicates that the spatial resolution used here (D/Δx = 10) is adequate for the present set of physical parameters.

The vertical profile of the streamwise velocity is presented for both phases at time $t(g/D)^{1/2} = 102$ in figure 12a. As expected, the velocity in the fluid is maximum at the top boundary (recall that a free-slip condition is imposed), with a strong decrease as one goes down to the surface of the granular bed, where the viscous shear is maximum. Variations of the fluid velocity are still observed inside the bed while the fluid velocity is vanishing as one approaches the bottom wall. The particle velocity is found to be of the same order of magnitude as that of the fluid at the same vertical location. Interestingly, the particle velocity is slightly but noticeably larger than that of the fluid at $0 \leq z/D \leq 6$, suggesting that the fluid is entrained by the particles in this region (as in a flow of avalanche type), while particles and fluid velocities are almost identical in the region $6 \leq z/D \leq 7$, indicating a transport of erosion type. This is line with the results of figure 12b, where the flow regime of the present simulation is plotted in the parameter space defined by the angle of inclination β and the Shields number $\theta = \mu\dot{\gamma}/(\rho_p - \rho_f)g\,D$, $\dot{\gamma}$ being the vertical fluid velocity gradient at the bed surface and μ the dynamic viscosity of the fluid. Loiseleux et al. [23] performed experiments in order to investigate the onset of erosion and avalanche for an inclined granular bed sheared by a continuous laminar flow, and found five flow regimes depending on these parameters, namely no motion (I), erosion (II), avalanche (III), and both erosion and avalanche (IV-V). Our present simulation lies in the regime II (erosion), close to the frontier between regimes II and V, suggesting that both erosion and avalanche are likely to play a role in the transport of particles.

5. CONCLUSIONS

We presented a simple soft-sphere immersed-boundary method capable of describing the flow of a three-dimensional dense granular media evolving in a viscous fluid. Both methods separately are able to accurately reproduce available experimental and numerical data. Simulations of wall-particle collisions in a fluid are shown to be in good agreement with experiments for the whole range of investigated parameters, provided that a local lubrication model is used. Simulations of gravity- and shear-driven dense granular flows in a viscous fluid were presented and a comparison was attempted with experiments. In the investigated regime of mixed erosion-avalanche, the

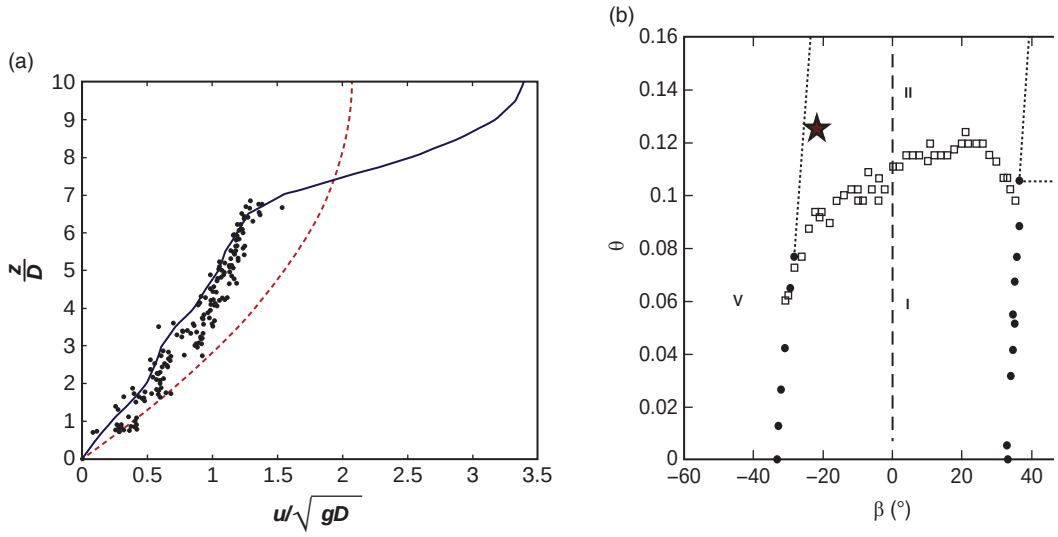

Figure 13: (a) Particles and fluid streamwise velocity as a function of height at $t(g/D)^{1/2} \approx 102$: •, particles velocity; —, fluid velocity averaged along the streamwise and spanwise directions, respectively; - - -, Poiseuille flow profile with no particle (divided by 10) (b) Type of granular transport in the parameter space (β, θ) corresponding to the angle of inclination and Shields number, respectively: ☆, present simulation; other symbols, experiments of [23] . These authors observed five regimes of transport, namely (I) no motion, (II) erosion, (III) avalanche, and (IV)-(V) erosion + avalanche. The shields number for the present simulation was computed at time $t(g/D)^{1/2} \approx 102$.

surface of the granular bed becomes unstable and ripples are formed. The wavelength of the surface pattern is of the computational domain size, and simulations in larger size domains are needed to obtain quantitative prediction of this granular flow quantity. Notwithstanding the somewhat modest spatial resolution used in the present work, the results open the way for a parametric study in the parameter space initial aspect ratio - initial packing with a larger number of better-resolved particles, in order to investigate immersed granular avalanches encountered in real situations.

ACKNOWLEDGEMENTS

The authors thank Annaig Pedrono for her support in the development of the immersed-boundary version of the Navier-Stokes solver used in this research. Some of the computational time was provided by the Scientific Groupment CALMIP (project P1027), the contributions of which is greatly appreciated.

REFERENCES

[1] Peskin, C. 2000 The immersed boundary method. *Acta Numerica* **11,** 479–517.

[2] Fadlun, E. A., Verzicco, R. Orlandi, P. & Mohd-Yusof, J. 2000 Combined immersed boundary finite-difference methods for three-dimensional complex flow simulations. *J. Comput. Phys.* **161**, 35–60.

[3] Kim, J., Kim, D. & Choi, H. 2001 An immersed-boundary finite-volume method for simulations of flow in complex geometries. *J. Comput. Phys.* **171**, 132–150.

[4] Uhlmann, M. 2005 An immersed boundary method with direct forcing for the simulation of particulate flows. *J. Comput. Phys.* **209**, 448–476.

[5] Bigot B., Bonometti T., Lacaze L. and Thual O. 2014 A simple immersed-boundary method for solid-fluid interaction in constant- and stratified-density flows. *Comput. Fluids* **97**, 126–142.

[6] Yuki, Y., Takeuchi S. & Kajishima, T. 2007 Efficient immersed boundary method for strong interaction problem of arbitrary shape object with self-induced flow. *J. Fluid Sci. Tech.* **2**, 1–11.

[7] Cundall, P.D. & Strack, O.D.L. 1979 A discrete numerical model for granular assemblies. *Geotechnique* **29**, 47

[8] Foerster, S. F., Louge, M. Y., Chang, A. H. & Allia, K. 1994 Measurements of the collision properties of small spheres. *Phys. Fluids* **6**, 1108–1115.

[9] Kempe, T. & Fohlich, J. 2012 Collision modelling for the interface-resolved simulation of spherical particules in viscous fluids, *J. Fluid Mech*, **709**, 445–489.

[10] Brenner, H. 1961 The slow motion of a sphere through a viscous fluid towards a plane surface. *Chem. Eng Sci*. **16**, 242–251.

[11] Joseph, G., Zenit, R., Hunt, L. & Rosenwinkel, M. 2001 Particule-wall collisions in a viscous fluid, *J. Fluid Mech*. **433**, 329–346.

[12] Mougin, G. & Magnaudet, J. 2001 Path instability of a rising bubble. *Phys. Rev. Lett*. **88**, 014502.

[13] Clift, R., Grace, J. R. & Weber, M. E. 1978 . In *Bubbles Drops and Particules*. Academic Press.

[14] Schäfer, J. 1996 Force schemes in simulations of granular materials, *J. Phys. I France* **6**, 5–20.

[15] Goldhirsch, I. & Goldenberg, C. 2002 On the microscopic foundations of elasticity, *Eur. Phys. J. E*. **9**, 245–251.

[16] Staron, L., & Hinch, J. 2005 Study of the collapse of granular columns using two-dimensional discrete-grain simulation, *J. Fluid Mech*. **545**, 1–27.

[17] Lacaze, L., Phillips, J.C. & Kerswell, R.R. 2008 Planar collapse of a granular column: Experiments and discrete element simulations. *Phys. of Fluids*. **20**, 063302.

[18] Girolami, L., Hergault, V., Vinay, G. & Wachs, A. 2012 A three-dimensional discrete-grain model for the simulation of dam-break rectangular collapses: comparison between numerical results and experiments. *Granular Matter.* **14**, 381–392.

[19] Gondret, P., Lance, M. & Petit, L. 2002 Bouncing motion of spherical particles in fluid, *Phys. Fluids* **14**, 643–652.

[20] Legendre, D., Daniel, C. & Guiraud, P. 2005 Drop-wall bouncing in a liquid, *Phys. of Fluids*, **17**, 97–105.

[21] Richard, D. & Quéré D. 2000 Bouncing water drops. *Eurphysics Letters* **50**, 769–775.

[22] Courrech du Pont, S., Gondret, P., Perrin, B., & Rabaud, M. 2003 Granular avalanches in fluids, *Phys. Rev. Lett*. **90**, 044301.

[23] Loiseleux, T., Gondret, P., Rabaud, M. & Doppler, D., 2005 Onset of erosion and avalanche for inclined granular bed sheared by a continuous laminar flow, *Phys. Fluids* **17**, 103304.